International Multilingual Journal of Science and Technology (IMJST)
ISSN: 2528-9810
Vol. 6 Issue 4, April - 2021

Analysis And Modelling Of Pitch And Plunge For Voltage And Power In Piezoelectric Harvesters

Umoren Ifiok Anthony
School of Computing, Engineering and Physical Sciences,
University of the West of Scotland, United Kingdom
Email: ifiok.umoren@uws.ac.uk

***Abstract*— This paper presents the modelling of the piezoelectric energy harvester beam to operate in pitch and plunge motion with a view to evaluating the performance analyses of the modelled piezoelectric energy harvester. The airfoil for the plunge and pitch motion models were derived using first principles techniques. Analyses of the steady state pitch and plunge voltage and current First Resonance Frequencies of the damped bimorph for a broad range of load resistance were carried out. The piezo-aeroelastic energy harvester gave an appreciable improvement in power generation at low wind speed capable of supporting many wireless sensor applications**.

Keywords*— *Piezoelectric, Wireless Sensor, Steady State Pitch, Plunge Motion, Resonance Frequencies, Energy Harvester, Damped Bimorph

I. INTRODUCTION

Energy harvesting is the process of extracting small amount of energy from ambient environment through various sources of energy. Energy harvesting is not a new concept; in essence it has been practiced for decades in the context of windmills to harness energy from wind, in hydroelectric generators to harvest energy from moving water, and in solar panels that draw energy from the sun. However, what is new with energy harvesting technology is how to design and implement efficient energy harvesting techniques into modern embedded systems while satisfying all their constraints (Rizman *et al.*, 2018; Hu *et al.*, 2018; Podder *et al.*, 2016). For any energy harvesting system to be considered attractive, it should allow miniaturization and integration using the present MEMS technology, otherwise it is not very useful. Eruk and Inman (2011) reported that mechanical energy in form of ambient vibrations, fluid flow, machine rotations, and biomotion presents a source of energy that is available widely and at all times. Piezoelectric materials can be used to harvest this energy since they have the unique ability of converting mechanical strain energy into useful electrical energy (Sarker *et al.*, 2016; Harne and Wang, 2016; Zeng *et al.*, 2016; Ono *et al.*, 2016).

Traditionally, batteries are used as the electrical energy power sources to power wireless sensors and embedded electronics. However, batteries have a limited life span and they are expensive to maintain and hence they are not a long-term viable source of energy for WSNs and embedded systems. In fact, the limited capacity of batteries is one of the main factors constraining the performance and limiting the lifespan of a typical WSN (Adhikari *et al.*, 2009). Energy harvesting is the most promising way of overcoming the challenges currently presented by finite life power sources like batteries. The process of energy harvesting involves the harnessing of ambient energy from within the vicinity of the sensor device and converting this energy into usable electrical energy. Compared to batteries, energy harvesting presents a potentially infinite source of energy for powering wireless sensor devices and embedded electronics in general (Briscoe and Dunn, 2014; Alper, 2009).

In recent years, piezoelectric energy harvesting has been setting the pace in energy scavenging due to its many advantages. Piezoelectric energy harvesters are devices that convert ambient environmental vibration into electrical energy by absorbing ambient vibrations (Kiran *et al*., 2014; Yuan *et al.*, 2018).

II. DERIVATION OF AIRFOIL PLUNGE AND PITCH MOTION

It is important to know how the aerodynamic forces, impact the behavior of the piezoelectric beam attached at the trailing edge of the airfoil. In order to study the aeroelastic behavior of the airfoil, the aerodynamic forces acting on the airfoil shall first be obtained by considering a quasi-steady condition.

Alighanbari (1995) in his work developed the lift and moment generated by a 2D airfoil under quasi-steady state conditions as:

$$L(h,\alpha) = \pi\rho c^2(h'' + V\alpha' - c\alpha_h\alpha'') + 2\pi\rho VcC(k)\left[h + V\alpha + c\dot{(}0.5 - \alpha_h)\alpha'\right] \quad (1)$$

$$M(h,\alpha) = \pi\rho c^2\left[c\alpha_h h'' - Vc(0.5 - \alpha_h)\alpha' - c^2\left(\frac{1}{8} + \alpha_h^2\right)\alpha''\right] + 2\pi\rho Vc^2(0.5 + \alpha_h)C(k)\left[h + V\alpha + c\dot{(}0.5 - \alpha_h)\alpha'\right] \quad (2)$$

where ρ is air density, c is the length of the airfoil semi-chord, μ is the airfoil-air mass ratio, V is the velocityof air speed, α_h is the nondimensional distance measured from airfoil mid-chord to elastic axis, $C(k)$ is the Theodorsen function, α is the pitch angle of the airfoil, prime denotes differentiation with respect to non-dimensional time, $k$is a complex function of reduced frequency ($k = \frac{\omega c}{V}$)and ω is the frequency of oscillations. If the NASA Langley rational function is adopted herewith as given by Jeffrey (1990), then an approximate rational function for $C(k)$ is expressed as:

$$C(k) = A_0 + A_1 ik + A_2 ik^2 + \frac{A_3 ik}{ik+b_1} + \frac{A_4 ik}{ik+b_2} + \frac{A_5 ik}{ik+b_3} + \frac{A_6 ik}{ik+b_4} \quad (3)$$

where $b_1 = 0.014919$, $b_2 = 0.080715$, $b_3 = 0.238540$, $b_4 = 0.687273$, $A_0 = 0.998585$, $A_1 = -0.000078$, $A_2 = 0.000012$, $A_3 = -0.040125$, $A_4 = -0.152297$, $A_5 = 0.227080$, and $A_6 = -0.078005$.

If the effect of vortex shedding induced by the uncoupled beam section is factored into Equation 1 and Equation 2, the lift and pitching moments is then expressed as:

$$L(h,\alpha) = \pi\rho c^2(h'' + V\alpha' - c\alpha_h\alpha'') + 2\pi\rho VcC(k)\left[h + V\alpha + c\dot{(}0.5 - \alpha_h)\alpha'\right] + L_v, \quad (4a)$$

$$M(h,\alpha) = \pi\rho c^2\left[c\alpha_h h'' - Vc(0.5 - \alpha_h)\alpha' - c^2\left(\frac{1}{8} + \alpha_h^2\right)\alpha''\right] + 2\pi\rho Vc^2(0.5 + \alpha_h)C(k)\left[h + V\alpha + c\dot{(}0.5 - \alpha_h)\alpha'\right] + M_v \quad (4b)$$

where L_v and M_v are vortex induced lift and moment of the uncoupled piezoceramic cantilever beam.

Considering the effect mass of the uncoupled beam and the lift vortex sheet generated by the attached piezoelectric cantilever beam. Since the vortex force opposes the accelerating force of the uncoupled section of the airfoil, the resultant effect of the forces is given as the summation of the sectional attached mass and vortex lift force as:

$$L_h = -\frac{\rho c^2\gamma^2}{72\pi h}\sin\theta - \rho_c\frac{c^3}{108}h'' \quad (5)$$

According to Anderson (2001), the pitching moment of vortex taken about the airfoil elastic axis is given by:

$$M_v = \frac{\rho c\gamma^2}{12\pi\alpha} \quad (6)$$

where α is the pitch angle, ρ is air density, γ is vortex strength per unit length and c is the semi-cord.

Hence, the lift and pitching moment generated by the aeroelastic system with vortex shedding effects of uncoupled airfoil are:

$$L_s(h,\alpha) = \pi\rho c^2(h'' + V\alpha' - c\alpha_h\alpha'') + 2\pi\rho VcC(k)\left[h + V\alpha + c\dot{(}0.5 - \alpha_h)\alpha'\right] - \left(\frac{\rho c^2\gamma^2}{72\pi h}\sin\theta + \rho_c\frac{c^3}{108}h''\right) \quad (7)$$

$$M_s(h,\alpha) = \pi\rho c^2\left[c\alpha_h h'' - Vc(0.5 - \alpha_h)\alpha' - c^2\left(\frac{1}{8} + \alpha_h^2\right)\alpha''\right] + 2\pi\rho Vc^2(0.5 + \alpha_h)C(k)\left[h + V\alpha + c\dot{(}0.5 - \alpha_h)\alpha'\right] + \frac{\rho c\gamma^2}{12\pi\alpha} \quad (8)$$

III. RESPONSE OF AIRFOIL HEAVING AND PITCHING MOTIONS

In other to derive the forced response when the system is subjected to a series of harmonic excitations, the steady state Frequency Response Function (FRF) for plunge can be derived from Equation 7 and Equation 8. This is achieved by equating the two lifts equations (Euqation 8 and Equation 7) and rearranging the resulting equation so that $\xi(\tau)$ and $\alpha(\tau)$ are separated on either side of the equation, then the equationis expressed as:

$$\left[\ell_{h1} + \pi e_1\rho c^3 + \frac{e_1\rho_c c^4}{108}\right]\xi''(\tau) + \zeta_\xi\frac{1}{U}\xi'(\tau) + \left[\ell_{h4} - 2\pi e_1\rho Vc^2C(k)\right]\xi(\tau) + \left[\ell_{h2} - \frac{e_1\rho c\gamma^2}{72\pi}\right]\xi(\tau)^{-1} = \left[\ell_{h3}x_\alpha - \pi e_1\rho c^3\alpha_h\right]\alpha''(\tau) + 2\pi e_1\rho Vc^2(0.5 - \alpha_h)C(k)\alpha'(\tau) + 2\pi e_1\rho cV^2C(k)\alpha(\tau) \quad (9)$$

where $e_1 = c^2/_{m_a U^2}$

Rewriting the left hand side of Equation 9 in the following standard form as:

$$a\xi''(\tau) + 2\zeta_\xi^*\omega_h^*\xi'(\tau) + \omega_h^{*2}\xi(\tau) + N_v^*\xi(\tau)^{-1} = \left[\ell_{h3}x_\alpha - \pi e_1\rho c^3\alpha_h\right]\alpha''(\tau) + 2\pi e_1\rho Vc^2(0.5 - \alpha_h)C(k)\alpha'(\tau) + 2\pi e_1\rho cV^2C(k)\alpha(\tau) \quad (10)$$

where $\omega_h^* = \sqrt{\left[\ell_{h4} - 2\pi e_1\rho Vc^2C(k)\right]}$, $\zeta_\xi^* = \frac{\zeta_\xi}{2\omega_h^* U} = \frac{\zeta_\xi}{2U\sqrt{\left[\ell_{h4} - 2\pi e_1\rho Vc^2C(k)\right]}}$, $a = \left[\ell_{h1} + \pi e_1\rho c^3 + \frac{e_1\rho_c c^4}{108}\right]$ and $N_v^* = \left[\ell_{h2} - \frac{e_1\rho c\gamma^2}{72\pi}\right]$.

In order to transform the pitching force components on the right hand side of Equation 10, a pitching displacement of the exponential function is assumed as:

$$\alpha(\tau) = \alpha_0 e^{\omega_\alpha\tau} \quad (11)$$

All the pitching motion components in Equation 10 will be replaced by Equation 11, (that is its first and second derivatives $\alpha'(\tau) = \omega_\alpha\alpha_0 e^{\omega_\alpha\tau}$ and $\alpha''(\tau) = \alpha_0\omega_\alpha^2 e^{\omega_\alpha\tau}$. Therefore, if these are substituted in Equation 3.35, then:

$$a\xi''(\tau) + 2\zeta_\xi^*\omega_h^*\xi'(\tau) + \omega_h^{*2}\xi(\tau) + N_v^*\xi(\tau)^{-1} = \left[\ell_{h3}x_\alpha - \pi e_1\rho c^3\alpha_h\right]\alpha_0\omega_\alpha^2 e^{\omega_\alpha\tau} + 2\pi e_1\rho Vc^2(0.5 - \alpha_h)C(k)\alpha_0\omega_\alpha e^{\omega_\alpha\tau} + 2\pi e_1\rho cV^2C(k)\alpha_0 e^{\omega_\alpha\tau} \quad (12)$$

In Equation 3.37, the solution is that of a forced vibration response since the airfoil is dynamically excited. The initial conditions induced a free vibration ξ_0 at the initial heaving motion and the solution consists of the following components.

$$\xi = \xi_0 + \xi_1 + \xi_2 + \xi_3 \quad (13)$$

Assuming $\xi_0 = 0$, (free vibration) and:

$$a\xi_1''(\tau) + 2\zeta_\xi^*\omega_h^*\xi_1'(\tau) + \omega_h^{*2}\xi_1(\tau) + N_v^*\xi_1(\tau)^{-1} = \left[\ell_{h3}x_\alpha - \pi e_1\rho c^3\alpha_h\right]\alpha_0\omega_\alpha^2 e^{\omega_\alpha\tau} \quad (14)$$

The solution of the nonhomogeneous ordinary differential equation (ODE) in Equation 14 is made up of both the homogeneous and particular solutions. Hence, the solution of the first component is:

$$\xi_1 = \xi_{1H} + \xi_{1P} \quad (15)$$

The homogeneous or complementary equation is:

$$a\xi_1''(\tau) + 2\zeta_\xi^*\omega_h^*\xi_1'(\tau) + \omega_h^{*2}\xi_1(\tau) + N_v^*\xi_1(\tau)^{-1} = 0 \quad (16)$$

Assuming the solution of Equation 16 is of the form $\xi_1(\tau) = \xi_0 e^{\lambda\tau}$, and differentiating the equation up to the second derivatives:

$$\xi_1(\tau) = \xi_0 e^{\lambda\tau}, \quad \xi_1'(\tau) = \xi_0\lambda e^{\lambda\tau}, \xi_1''(\tau) = \xi_0\lambda^2 e^{\lambda\tau} \quad (17)$$

Substituting Equation 16 into Equation 17 and rearranging:

$$\xi_0 e^{\lambda\tau}\left[a\lambda^2 + 2\zeta_\xi^*\omega_h^*\lambda + \omega_h^{*2}\right] = -\frac{1}{\xi_0}N_v^* e^{-\lambda\tau} \quad (18)$$

Multiplying Equation 18 through by $e^{\lambda\tau}$

$$e^{2\lambda\tau}\left[a\lambda^2 + 2\zeta_\xi^*\omega_h^*\lambda + \omega_h^{*2} + N_v^*\right] = \xi_0^{-2} \quad (19)$$

The resulting characteristic equations are:

$$e^{2\lambda\tau} = \xi_0{}^{-2},\ a\lambda^2 + 2\zeta_\xi^*\omega_h^*\lambda + (\omega_h^{*2} + N_v^*) = 0 \quad (20)$$

The first part of Equation 20 is not a valid characteristic equation since it will not yield valid roots. This is why the solution and roots determination were done using only the second part of the equation. Using the quadratic equation formula ($x = \frac{-b\pm\sqrt{b^2-4ac}}{2a}$) to find the roots of Equation 20. Therefore the roots of the quadratic equation in Equation 20 are:

$$\lambda_1 = -{}^1/_a\,\zeta_\xi^*\omega_h^* + {}^1/_{2a}\sqrt{4\zeta_\xi^{*2}\omega_h^{*2} - 4a(\omega_h^{*2} + N_v^*)},$$

$$\lambda_2 = -{}^1/_a\,\zeta_\xi^*\omega_h^* - {}^1/_{2a}\sqrt{4\zeta_\xi^{*2}\omega_h^{*2} - 4a(\omega_h^{*2} + N_v^*)} \quad (21)$$

The values of the roots in Equation 3.46 are not constant and this will determine to a greater extent what the response of the plunge motion of the airfoil will be. This shows that the critical damping, ζ_ξ^*, circular frequencies ω_h^* and vortex aerodynamic load N_v^* of the system plays a very important role in determining the nature of heaving motion of the airfoil, and their values should be chosen with care in order to obtain better results. Since the roots are unequal, the general solution of the homogeneous part of ξ_1, is the sum of the two solution components, where $A$and $B$are constants of plunge homogeneous equation.

$$\xi_{1H} = Ae^{\lambda_1\tau} + Be^{\lambda_2\tau} \quad (22)$$

The particular solution of ξ_1, needs to be form, by choosing a function similar to $f(\tau) = [\ell_{h3}x_\alpha - \pi e_1\rho c^3\alpha_h]\alpha_0\omega_\alpha^2 e^{\omega_\alpha\tau}$. In forming the particular solution ξ_{1P}, it should be noted that $f(\tau)$ is the right hand side of Equation 14. $\xi_{1P} = Ce^{\omega_\alpha\tau}$ was proposed for the particular solution and if the derivatives of the equation are taken up to the second differential, then:

$$\xi_{1P} = Ce^{\omega_\alpha\tau},\ \xi_{1P}{}' = \omega_\alpha Ce^{\omega_\alpha\tau},\ \xi_{1P}{}'' = \omega_\alpha{}^2Ce^{\omega_\alpha\tau} \quad (23)$$

Substitute the components of Equation 23 in Equation 14, and rearrange accordingly, then:

$$\left[a\omega_\alpha{}^2 + 2\zeta_\xi^*\omega_h^*\omega_\alpha + \omega_h^{*2}\right]Ce^{2\omega_\alpha\tau} + \frac{N_v^*}{C} = [\ell_{h3}x_\alpha - \pi e_1\rho c^3\alpha_h]\alpha_0\omega_\alpha^2 e^{2\omega_\alpha\tau} \quad (24)$$

Solving for the value of the constant, C.

$$\frac{N_v^*}{C} = 0,\quad C = \frac{[\ell_{h3}x_\alpha - \pi e_1\rho c^3\alpha_h]\alpha_0\omega_\alpha^2}{\left[a\omega_\alpha{}^2 + 2\zeta_\xi^*\omega_h^*\omega_\alpha + \omega_h^{*2}\right]}$$

Equation 25

From Equation 25, only valid value for particular solution is the nonzero value of C, and hence:

$$\xi_{1P} = \frac{[\ell_{h3}x_\alpha - \pi e_1\rho c^3\alpha_h]\alpha_0\omega_\alpha^2}{\left[a\omega_\alpha{}^2 + 2\zeta_\xi^*\omega_h^*\omega_\alpha + \omega_h^{*2}\right]}e^{\omega_\alpha\tau} \quad (25)$$

The solution of the first component of the heaving motion is:

$$\xi_1 = \xi_{1H} + \xi_{1P},$$

$$\xi_1 = Ae^{\lambda_1\tau} + Be^{\lambda_2\tau} + \frac{[\ell_{h3}x_\alpha - \pi e_1\rho c^3\alpha_h]\alpha_0\omega_\alpha^2}{\left[a\omega_\alpha{}^2 + 2\zeta_\xi^*\omega_h^*\omega_\alpha + \omega_h^{*2}\right]}e^{\omega_\alpha\tau} \quad (26)$$

In order to obtain the values for the constants A and B, respectively, the initial conditions of the system which states that at the time ($\tau = 0$) just before motion commences, the plunge displacement and velocity remains zero, would be applied. That is:

$$\xi_1(0) = 0,\ \xi_1{}'(0) = 0 \quad (27)$$

Substituting Equation 27 into Equation 26, we have:

$$A + B = -\frac{[\ell_{h3}x_\alpha - \pi e_1\rho c^3\alpha_h]\alpha_0\omega_\alpha^2}{\left[a\omega_\alpha{}^2 + 2\zeta_\xi^*\omega_h^*\omega_\alpha + \omega_h^{*2}\right]} \quad (28)$$

$$\lambda_1 A + \lambda_2 B = -\frac{[\ell_{h3}x_\alpha - \pi e_1\rho c^3\alpha_h]\alpha_0\omega_\alpha^3}{\left[a\omega_\alpha{}^2 + 2\zeta_\xi^*\omega_h^*\omega_\alpha + \omega_h^{*2}\right]} \quad (29)$$

From Equation 3.54, the expression of A, was obtained in terms of B.

$$A = -\frac{[\ell_{h3}x_\alpha - \pi e_1\rho c^3\alpha_h]\alpha_0\omega_\alpha^2}{\left[a\omega_\alpha{}^2 + 2\zeta_\xi^*\omega_h^*\omega_\alpha + \omega_h^{*2}\right]} - B \quad (30)$$

Substituting Equation 30 into Equation 29, then:

$$-\lambda_1\frac{[\ell_{h3}x_\alpha - \pi e_1\rho c^3\alpha_h]\alpha_0\omega_\alpha^2}{\left[a\omega_\alpha{}^2 + 2\zeta_\xi^*\omega_h^*\omega_\alpha + \omega_h^{*2}\right]} - (\lambda_2 - \lambda_1)B = \frac{\omega_\alpha[\ell_{h3}x_\alpha - \pi e_1\rho c^3\alpha_h]\alpha_0\omega_\alpha^2}{\left[a\omega_\alpha{}^2 + 2\zeta_\xi^*\omega_h^*\omega_\alpha + \omega_h^{*2}\right]} \quad (31)$$

Solving Equation 31, the expression for constant B, is:

$$B = \frac{(\omega_\alpha - \lambda_1)[\ell_{h3}x_\alpha - \pi e_1\rho c^3\alpha_h]\alpha_0\omega_\alpha^2}{(\lambda_2 - \lambda_1)\left[a\omega_\alpha{}^2 + 2\zeta_\xi^*\omega_h^*\omega_\alpha + \omega_h^{*2}\right]} \quad (32)$$

Also, substituting the value B in Equation 30, A can be expressed as:

$$A = \frac{(\omega_\alpha - \lambda_2)[\ell_{h3}x_\alpha - \pi e_1\rho c^3\alpha_h]\alpha_0\omega_\alpha^2}{(\lambda_2 - \lambda_1)\left[a\omega_\alpha{}^2 + 2\zeta_\xi^*\omega_h^*\omega_\alpha + \omega_h^{*2}\right]} \quad (33)$$

Substituting the values of A and B, in Equation 26, and with proper rearrangements, then:

$$\xi_1 = \frac{[\ell_{h3}x_\alpha - \pi e_1\rho c^3\alpha_h]\alpha_0\omega_\alpha^2}{\left[a\omega_\alpha{}^2 + 2\zeta_\xi^*\omega_h^*\omega_\alpha + \omega_h^{*2}\right]}\left\{\frac{(\omega_\alpha - \lambda_2)}{(\lambda_2 - \lambda_1)}e^{\lambda_1\tau} + \frac{(\omega_\alpha - \lambda_1)}{(\lambda_2 - \lambda_1)}e^{\lambda_2\tau} + e^{\omega_\alpha\tau}\right\} \quad (34)$$

In a similar manner, the other heaving motion components were obtained and expressed as:

$$\xi_2 = \frac{2\pi e_1\rho Vc^2(0.5 - \alpha_h)C(k)\alpha_0\omega_\alpha}{\left[a\omega_\alpha{}^2 + 2\zeta_\xi^*\omega_h^*\omega_\alpha + \omega_h^{*2}\right]}\left\{\frac{(\omega_\alpha - \lambda_2)}{(\lambda_2 - \lambda_1)}e^{\lambda_1\tau} + \frac{(\omega_\alpha - \lambda_1)}{(\lambda_2 - \lambda_1)}e^{\lambda_2\tau} + e^{\omega_\alpha\tau}\right\} \quad (35)$$

$$\xi_3 = \frac{2\pi e_1\rho cV^2C(k)\alpha_0}{\left[a\omega_\alpha{}^2 + 2\zeta_\xi^*\omega_h^*\omega_\alpha + \omega_h^{*2}\right]}\left\{\frac{(\omega_\alpha - \lambda_2)}{(\lambda_2 - \lambda_1)}e^{\lambda_1\tau} + \frac{(\omega_\alpha - \lambda_1)}{(\lambda_2 - \lambda_1)}e^{\lambda_2\tau} + e^{\omega_\alpha\tau}\right\} \quad (36)$$

In other to obtain, the heaving motion final frequency response function (FRF), the principle of superposition of waves forms were applied as already expressed in Equation 16, and by substituting the components in Equations 34, Equation 35, and Equation 36, into Equation 16 yeilds:

$$\xi = \frac{A^*\alpha_0}{\left[a\omega_\alpha{}^2 + 2\zeta_\xi^*\omega_h^*\omega_\alpha + \omega_h^{*2}\right]}\left\{\frac{e^{-1/a\,\zeta_\xi^*\omega_h^*\tau}}{(\lambda_2 - \lambda_1)}\left[2\omega_\alpha\sinh(w_f\tau) + (\lambda_1 e^{-w_f\tau} - \lambda_2 e^{w_f\tau})\right] + e^{\omega_\alpha\tau}\right\} \quad (37)$$

where $A^* = [\ell_{h3}x_\alpha - \pi e_1\rho c^3\alpha_h]\omega_\alpha^2 + 2\pi e_1\rho Vc^2(0.5 - \alpha_h)C(k)\omega_\alpha + 2\pi e_1\rho cV^2C(k)$, α_0 =1, $\sinh = \frac{e^{w_f\tau} - e^{-w_f\tau}}{2}$ and $w_f = {}^1/_{2a}\sqrt{4\zeta_\xi^{*2}\omega_h^{*2} - 4a(\omega_h^{*2} + N_v^*)}$

The same procedure was equally applied to the pitching motion forced response when the system is subjected to a series of harmonic excitations. This is expressed as:

$$\alpha = \frac{A^{**}\xi_0}{\left[a\omega_h{}^2 + 2\zeta_\alpha^*\omega_\alpha^*\omega_h + \omega_\alpha^{*2}\right]}\left\{\frac{e^{-1/a\,\zeta_\xi^*\omega_h^*\tau}}{(\lambda_1{}^* - \lambda_2{}^*)}\left[\left(\lambda_2{}^*e^{w_f{}^*\tau} - \lambda_1{}^*e^{w_f{}^*\tau}\right) - 2\omega_h sinh(w_f{}^*\tau)\right] + e^{\omega_h\tau}\right\} \quad (38)$$

where $A^{**} = \left[\left(\varkappa_{h1} + \frac{x_\alpha}{\tau_\alpha^2}\right) - \pi e_2 \rho c^4 \alpha_h\right] \omega_h^2 + \left[\varkappa_{h2} \left(\frac{\varpi}{U}\right)^2 - 2\pi e_2 \rho V c^3 (0.5 + \alpha_h) C(k)\right]$

$w_f{}^* = {}^1\!/_{2a} \sqrt{4\zeta_\alpha^{*2}\omega_\alpha^{*2} - 4a(\omega_\alpha^{*2} + N_v^{**})}$, $\xi_0 = 1$, $\omega_\alpha^* = \sqrt{\frac{1}{U^2} - 2\pi e_2 \rho V^2 c^2 (0.5 + \alpha_h)}$,

$\zeta_\alpha^* = \frac{\left[\zeta_\alpha \frac{1}{U} + \pi e_2 \rho V c^3 (0.5 - \alpha_h) - 2\pi e_2 \rho V c^3 (0.5 - \alpha_h)\right]}{2\sqrt{\frac{1}{U^2} - 2\pi e_2 \rho V^2 c^2 (0.5 + \alpha_h)}}$, $\lambda_1{}^* = -{}^1\!/_a \zeta_\alpha^* \omega_\alpha^* + {}^1\!/_{2a} \sqrt{4\zeta_\alpha^{*2}\omega_\alpha^{*2} - 4a(\omega_\alpha^{*2} + N_v^{**})}$, $\lambda_2{}^* = -{}^1\!/_a \zeta_\alpha^* \omega_\alpha^* - {}^1\!/_{2a} \sqrt{4\zeta_\alpha^{*2}\omega_\alpha^{*2} - 4a(\omega_\alpha^{*2} + N_v^{**})}$ and $\sinh = \frac{e^{wf\tau} - e^{-wf\tau}}{2}$.

IV. AEROELASTIC ENERGY HARVESTER RESULTS UNDER QUASI-STEADY AERODYNAMICS OF AIRFOIL BASE EXCITATION

The analysis given here considers the frequency range of 0 - 1000 Hz, and it can be shown that this cantilever has three vibration modes in this frequency range. In the previous section, the optimum aerodynamic parameters were determined for the quasi-steady excitation of the airfoil base structure. These aerodynamic parameters decide to a great extent how much voltage, current and power is generated by the piezoelectric energy harvester. Considering the first three vibration modes, the fundamental mode of vibration as shown in Figure 3, is accompanied with two strain nodes.

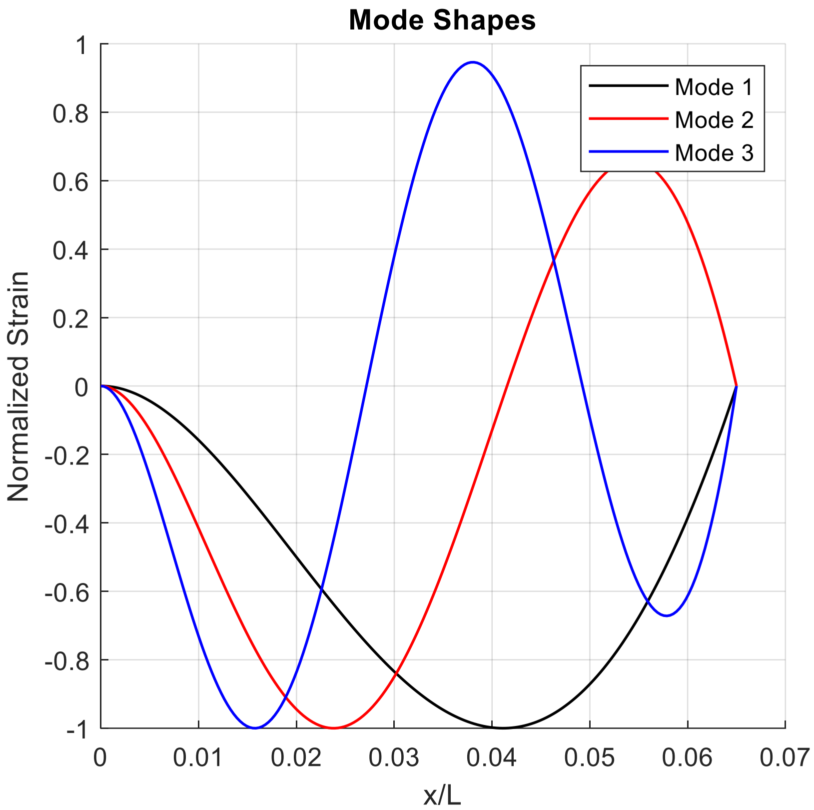

Figure 3: First three vibration mode shapes of the cantilevered beam energy harvester

Frequency Response of the Voltage Output under Quasi-Steady Aerodynamic Airfoil Base Excitation

The analytical simulation results are given in this section. The base of the cantilever is assumed to be rotating as the airfoil pitch under the influence of aerodynamic flutter. The series connection case is considered first. This analysis is carried out around the air flow speed with which flutter has been determined to have occurred. It is at this point that the aeroelastic system exhibits the highest level or quantity of vibratory energy. The set of electrical load resistance considered here ranges from $0.33\ T\Omega$ to $33\ P\Omega$. The lowest resistance ($R_l = 0.33\ T\Omega$) used here is very close to the short-circuit conditions while the largest load ($R_l = 33\ P\Omega$) is very close to the open-circuit conditions.

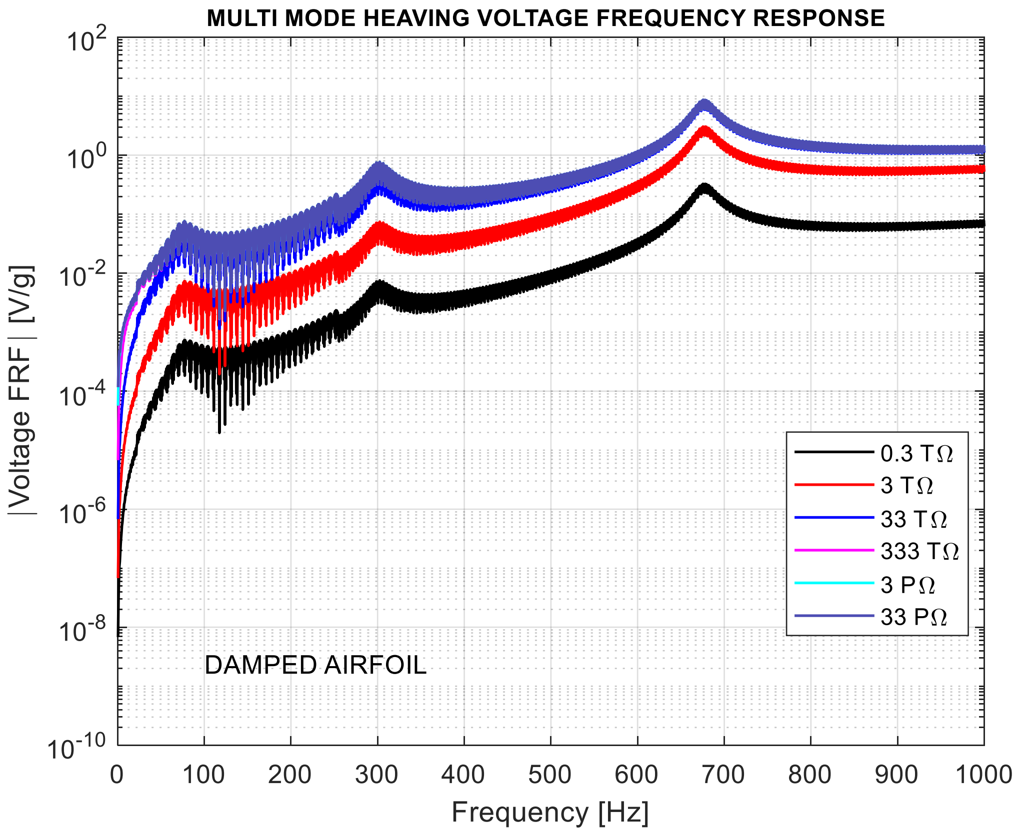

Figure 4: Steady state plunge voltage FRFs of the bimorph for a specific range of load resistance

The voltage output FRFs graphs in Figure 4, Figure 5 and Figure 6, shows the voltage FRFs when the base structure is undergoing flutter under quasi-steady conditions and otherwise known as the damped airfoil. The contribution of the plunge and pitch motions of the base acceleration, and superimposition of both constitute the total voltage produced by the harvester. In studying the behavior of the system, the load resistance is increased from short-circuit to open-circuit conditions, and this shows that the voltage output at each frequency increases. The short-circuit condition is defined as load resistance approaches $0.33\ T\Omega$ and the open-circuit condition defined as load resistance reaches $33\ P\Omega$. The simulation results showed that the load resistance range stipulated outside this range $(0.3\ T\Omega - 33\ P\Omega)$, cause the system not to attain resonance most especially at higher vibration modes, resulting in very low voltage generation. An important aspect of the voltage FRFs plotted in voltage output, which shows that at increasing the load resistance, the voltage output at each frequency converges to its maximum value as system attain each vibration mode's resonance. The short-circuit and open-circuit resonance frequencies of each vibration mode remain equally the same as one moves from the short-circuit load resistance (f_r^{SC} for $R_l \rightarrow 0.33\ T\Omega$) to the open-circuit load resistance (f_r^{OC} for $R_l \rightarrow 33\ P\Omega$).

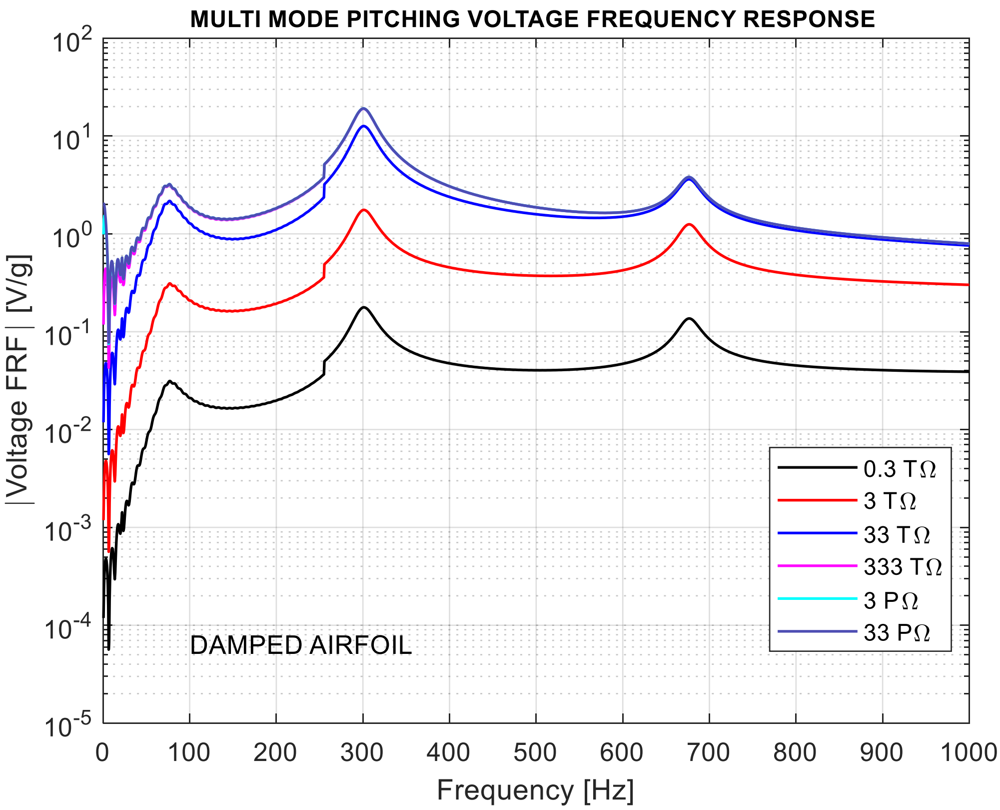

Figure 5: Steady state pitch voltage FRFs of the damped bimorph for a broad range of load resistance

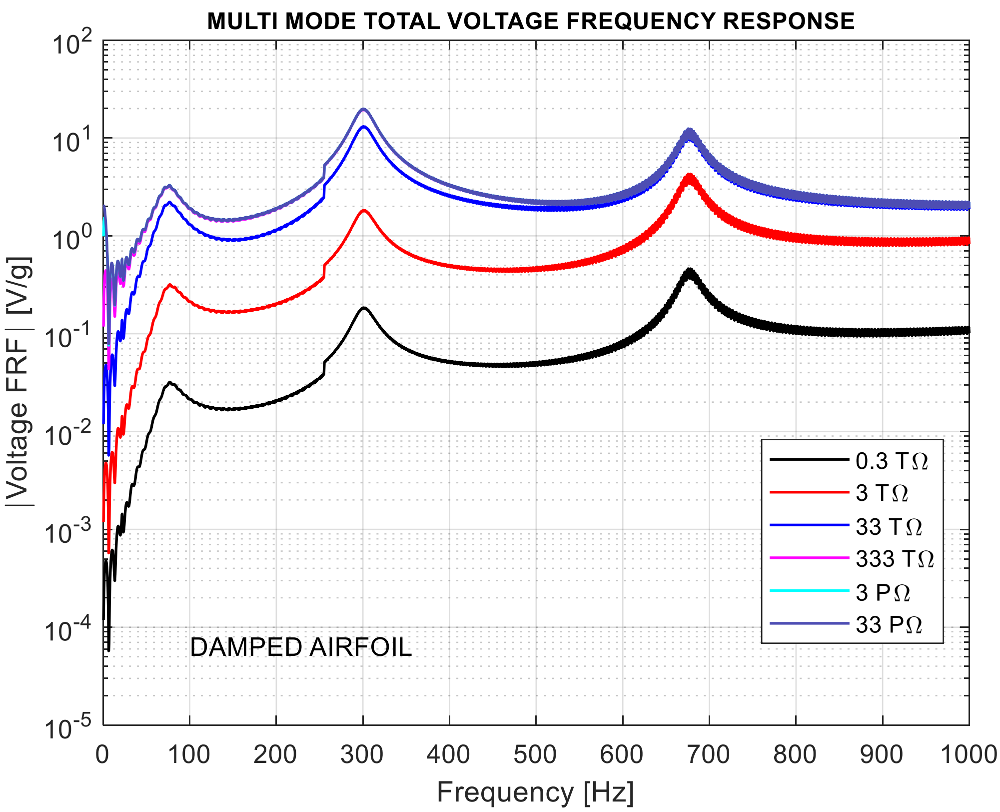

Figure 6: Steady state total voltage FRFs of the damped bimorph for a specific range of load resistance

It can be seen from the voltage output graphs (as shown in Figure 4, Figure 5 and Figure 6) that the voltage generated by a given piezoelectric energy harvester depends on the resonance frequency and external load resistance used in configuring the electrical circuit. The system reached its open-circuit condition at a load resistance of

$R_l = 333\ T\Omega$ for the plunge, pitch and system voltage FRFs responses. Short-circuit and open-circuit resonance frequencies of the first three modes are listed in Table 1.

Table 1: First three short-circuit and open-circuit resonance frequencies read from the voltage FRF of the bimorph piezoelectric aeroelastic energy harvester

Mode (r)	$f_r^{SC}[Hz]$	$f_r^{OC}[Hz]$
1	76.50	76.05
2	302.00	302.00
3	676.50	676.50

It is observed throughout the presentation of the voltage FRFs that the plunge motion contribution to the voltage FRFs output is basically higher than the pitch motion from aerodynamic excitation of the airfoil base structure under quasi-steady conditions. For the three mode of vibration, the maximum generated voltage output at each resonance frequency of the system is tabulated in Table 2. It can be seen from the results that the first mode does not produce maximum voltage due to interaction of the airfoil base aerodynamics with the structural dynamics of the piezoelectric cantilever beam. This lead to reshuffling or cancellation of the strain nodes along the beam's length, reducing and later progresses as vibration modes increases. For the plunge motion (as shown in Table 2), the third mode produces the highest voltage contribution ($V = 8650\ mV$) while the first contributes the least ($V = 7.56 mV$). It can be seen for the pitch motion, mode two registered a high voltage FRF output of $V = 19060 mV$ and mode one contributed just small voltage FRF value of $V = 3074\ mV$. In conclusion, the second mode that produce the highest voltage FRF output under quasi-steady conditions with a value of $V = 19210\ mV$.

Table 2: Maximum voltage FRFs output of the bimorph piezoelectric aeroelastic harvester at resonance frequencies of the first three modes

Mode (r)	$f_r[Hz]$	Plunge Voltage $[mV]$	Pitch Voltage $[mV]$	System Voltage $[mV]$
1	76.50	7.56	3074	3212
2	302.00	77.13	19060	19210
3	676.50	8650	3804	12400

The mechanical resonance frequency does not depend on the load resistance of the circuit neither does the electrical resonance frequency, rather it is strongly affected by the structural properties of the composite bimorph beam. In comparing, mode one mechanical resonance frequency is slightly lower than its counterpart short-circuit and open-circuit resonance frequency with $f_r = 75.96\ Hz$ and $f_r^{SC} = f_r^{OC} = 76.50\ Hz$. There is a different trend observed in the second mode of vibration, where it is discovered that the mechanical resonance frequency tends to be a bit lower than its corresponding short-circuit and open-circuit resonance frequencies with $f_r = 300.0\ Hz$, and $f_r^{SC} = f_r^{OC} = 302.0\ Hz$. The second mode of vibration of the base structure is the pitching of the airfoil wing, which is why this drop in electrical resonance frequency away from its equivalent mechanical resonance frequency is accompanied with a drop in voltage FRF output amplitude resulting from the airfoil pitch motion contribution as shown in Figure 1. In the third mode's electrical resonance frequency increases from its mechanical resonance frequency from $f_r = 676.0\ Hz$, to $f_r^{SC} = f_r^{OC} = 676.5\ Hz$ .This is a valid deduction from the analysis to say that the short-circuit and open-circuit resonance frequencies traced from the FRFs plot does not only depend on the load resistance, but also on the mechanical resonance frequency and mechanical damping of the piezoelectric cantilever beam.

Frequency Response of the Current Output under Quasi-Steady Aerodynamic Airfoil Base Excitation

In the simulations for current FRF given here, the current FRF is plotted against the frequency in Figure 7, Figure 8 and Figure 9. Unlike the voltage FRF (as shown in Figure 4, Figure 5 and Figure 6) the amplitude of the current at every frequency decreases with increasing load resistance. It can be seen that the current output trend is opposite of the voltage behavior shown in Figure 4, Figure 5 and Figure 6. As the airfoil is excited at every excitation frequency, the maximum value of the current is obtained when the system is close to short-circuit conditions and minimum when it is at open-circuit. In the region of relatively low load resistance, the current output is larger at the short-circuit resonance frequency which is contrary to the case of the voltage output, where the voltage output assumed much lower values at the system short-circuit conditions. Also, the current output progressively decreases with increasing load resistance.

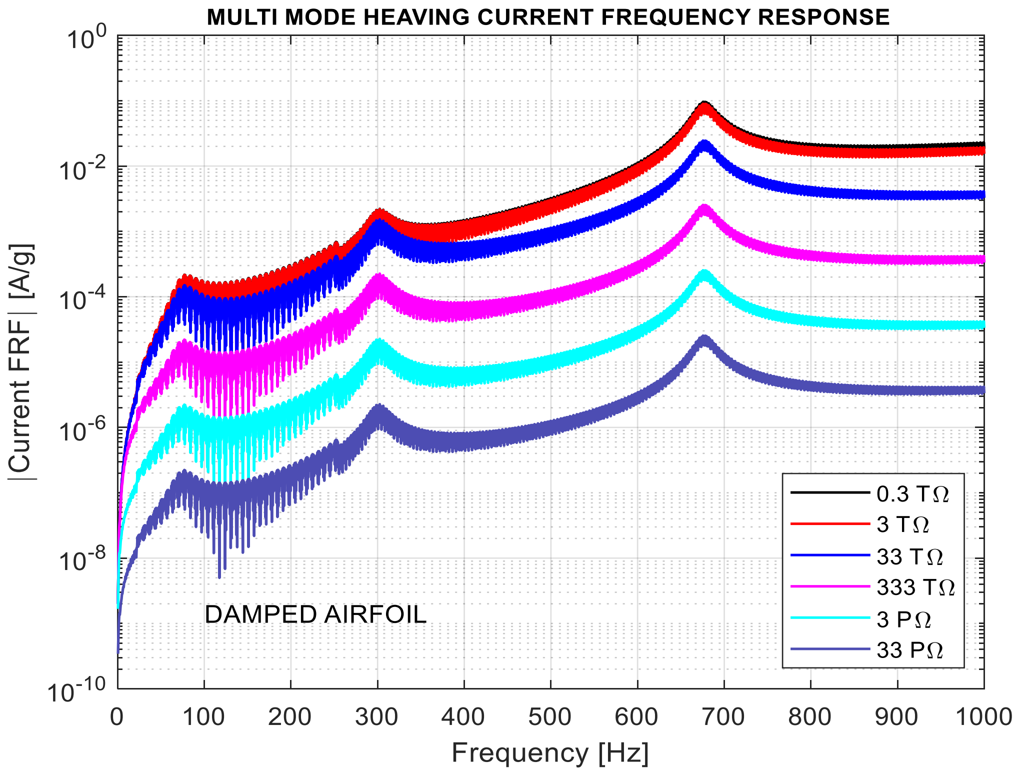

Figure 7: Steady state plunge current FRFs of the damped bimorph for a specific range of load resistance

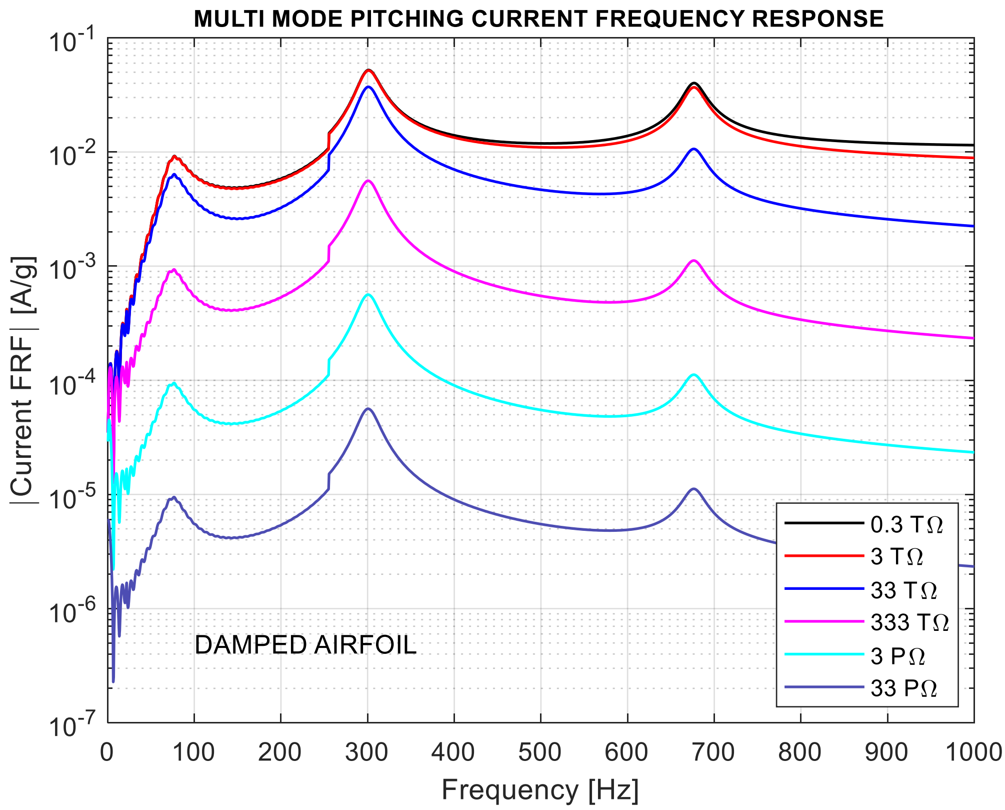

Figure 8: Steady state pitch current FRFs of the undamped bimorph for a specific range of load resistance

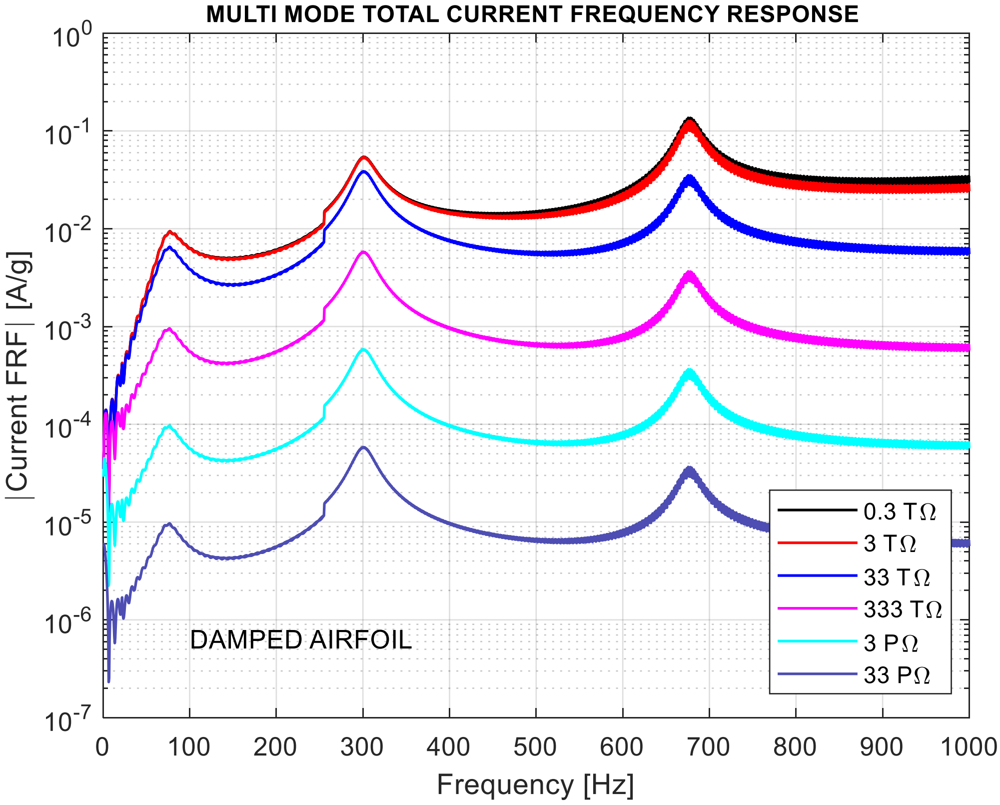

Figure 9: Steady state system current FRFs of the undamped bimorph for a specific range of load resistance

It is important to assess the current output contribution by plunge motion, and pitch motion to the current FRFs for aerodynamic excitation of the airfoil base structure under quasi-steady conditions. The maximum generated current output at each resonance frequency of the system for the three mode of vibration is tabulated in Table 3.

Table 3: Maximum current FRFs output of the bimorph piezoelectric aeroelastic energy harvester at resonance frequencies of the first three modes

Mode (r)	$f_r [Hz]$	Plunge Current $[mA]$	Pitch Current $[mA]$	System Current $[mA$
1	76.50	0.22	9.14	9.39
2	302.00	2.19	52.25	53.74
3	676.50	9.61	40.17	136.10

Table 3 indicates that the pitch motion contributes more current than the plunge motion of the airfoil base structure. The results shows that the first mode does not produce maximum current due to interaction of the airfoil base aerodynamics with the structural dynamics of the piezoelectric cantilever beam, and this behavior is similar to the one obtained in the voltage FRFs. For the plunge motion, the third mode produces the highest current contribution ($I = 9.61\,mA$) while the first mode contributes the least ($I = 0.22\,mA$). Considering the pitch motion, the second mode registered a high current FRF output of ($I = 52.25\,mA$) and mode one contributed lowest current FRF value of $I = 9.14\,mA$. Therefore it is the third mode of the system's current that produce the highest current FRF output under quasi-steady conditions with a value of $I = 136.10\,mA$.

Frequency Response of the Power Output under Quasi-Steady Aerodynamic Airfoil Base Excitation

In the simulations for power FRF presented in Figure 10, Figure 11 and Figure 12, the amplitude of the power output at different frequencies increases and decreases with increasing load resistance. The power output plots intermingles at the first, second and third resonance frequencies. As the airfoil is excited at every excitation frequency, the maximum value of the power is obtained when the system is close to short-circuit conditions and minimum when it is at open-circuit.

The maximum power output for the first vibration mode corresponds to the load of $33\,T\Omega$ (see Figure 10) at $76.5\,Hz$. In the second vibration mode of the pitch motion (see Figure 11), it is observed that the maximum power output is obtained for $33\,T\Omega$ at frequency $302.0\,Hz$, and the third mode a peak power at open-circuit load resistance of $3\,T\Omega$ and corresponding resonance frequency of $676.0\,Hz$ is achieved. The power FRFs given in Figure 12, that some of the power output plots, intersect one another along some of the load resistance curves. These intersections are observed around the resonance frequency of $76.5\,rad/s$, and off-resonance frequencies of $194.5\,rad/s$, $225\,rad/s$, and $654\,rad/s$, between curves of load resistances of $3\,T\Omega$ and $333\,T\Omega$. The intersecting curves are also observed at the off-resonance frequencies between curves of $3\,T\Omega$ and $33\,T\Omega$, and of $0.33\,T\Omega$ and $333\,T\Omega$. At these intersection frequencies, the two respective load resistance values, yield the same power FRF output.

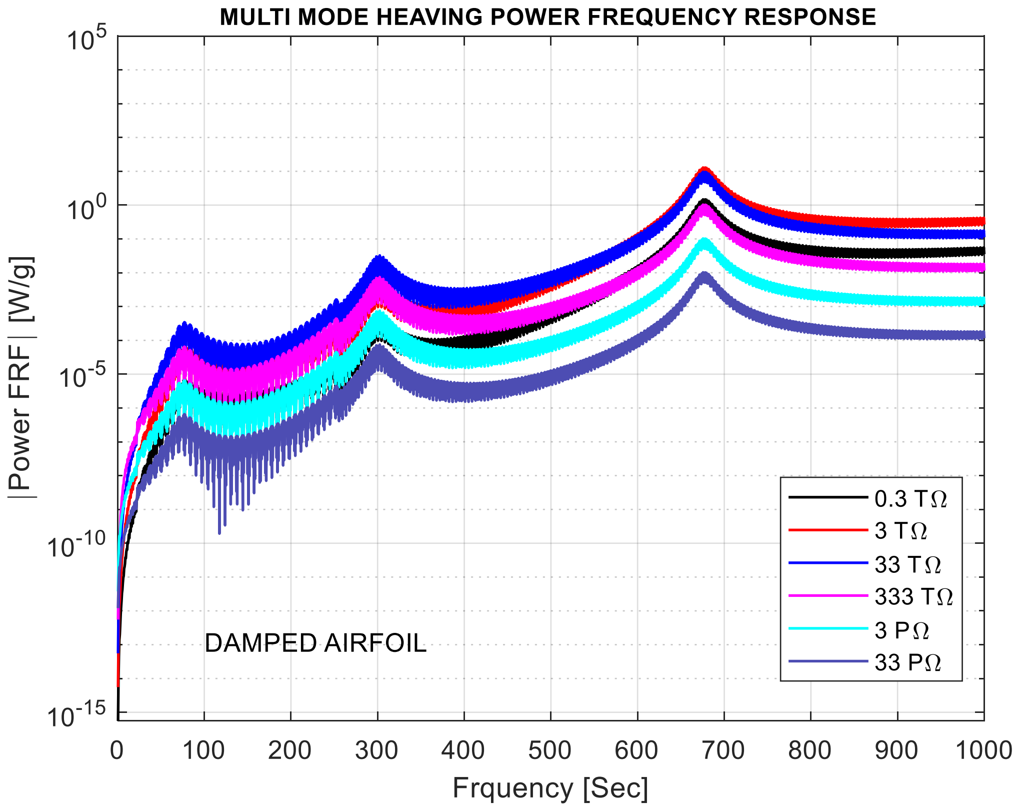

Figure 10: Steady state plunge power FRFs of the damped bimorph for a specific range of load resistance

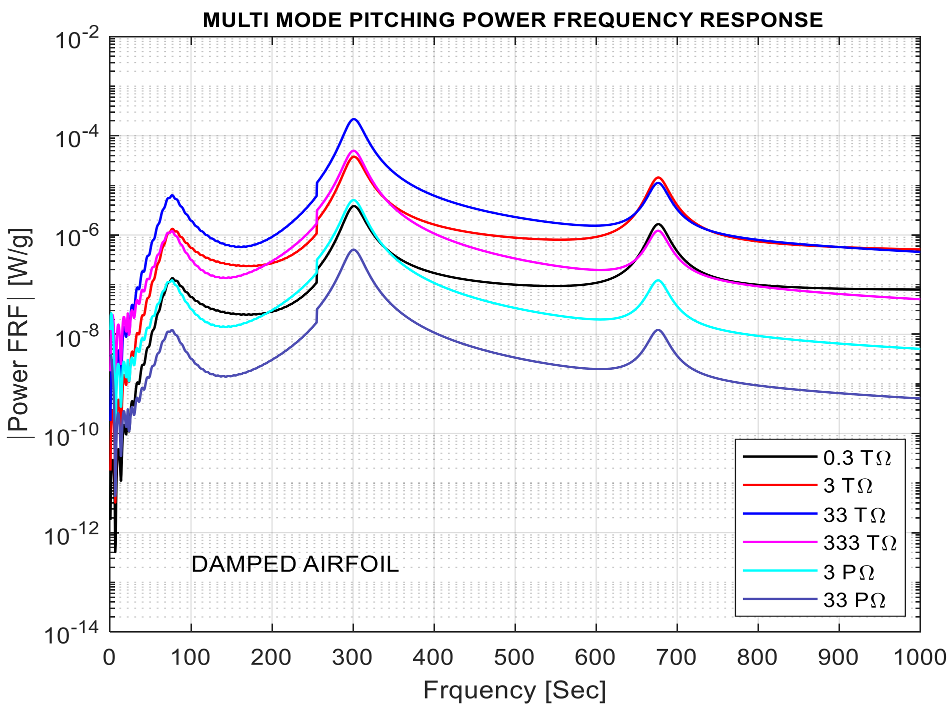

Figure 11: Steady state pitch power FRFs of the damped bimorph for a specific range of load resistance

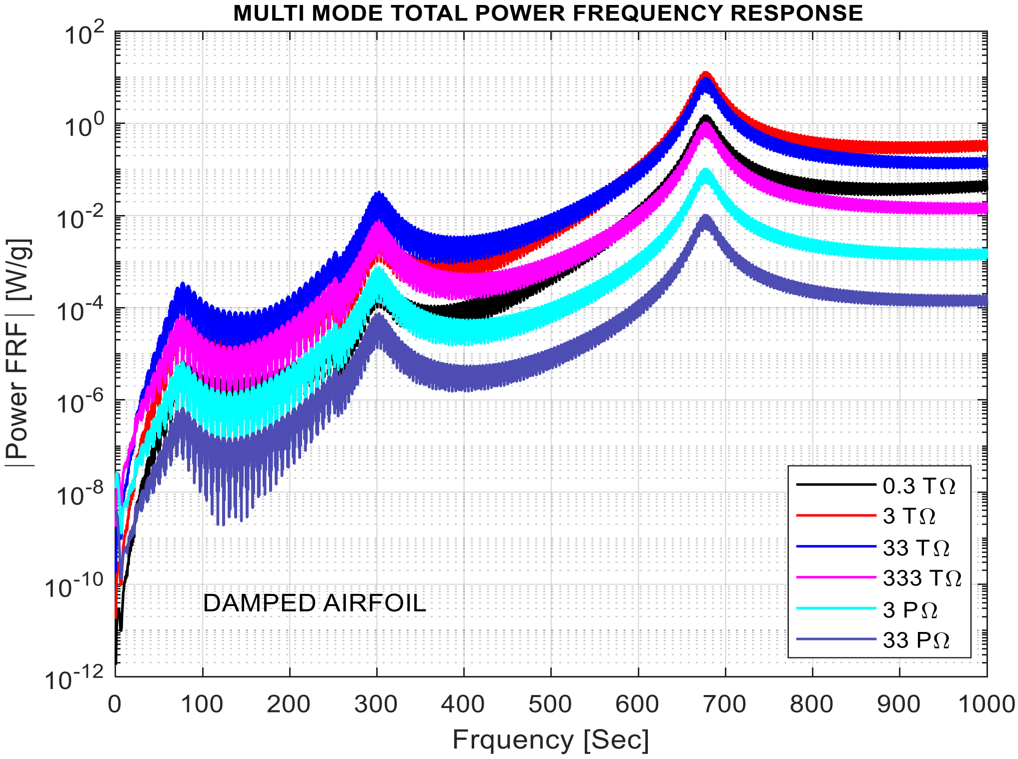

Figure 12: Steady state system power FRFs of the damped bimorph for a specific range of load resistance

It can be observed throughout the presentation of the power FRFs that the plunge motion contribution to the power FRFs output is basically higher than the pitch motion portion from aerodynamic excitation of the airfoil base structure under quasi-steady conditions. It can be seen in Table 4.14 that from the three mode of vibration, that maximum generated power output at each resonance frequency of the system is at the third mode of vibration.

Table 4: Maximum power FRFs output of the bimorph piezoelectric aeroelastic energy harvester at resonance frequencies of the first three modes

Mode (r)	$f_r[Hz]$	Plunge Power$[mW]$	Pitch Power$[mW]$	System Power$[mW]$
1	76.50	0.34	0.0063	0.35
2	302.00	32.50	0.22	32.71
3	676.50	12900	0.014	12900

It can be observed in the plunge motion, the third mode produces the highest power contribution ($P = 12900\,mW$) while the first mode contributes the least ($P = 0.34\,mW$). Similarly, for the pitch motion, mode two registered a high power FRF output of $P = 0.22\,mW$ and mode one contributed just small power FRF value of $P = 0.0063\,mW$. It is the third mode of the system power output that produces the highest power FRF output under quasi-steady conditions with a value of $P = 12900\,mW$.

V. CONCLUSION

This research developed and modelled distributed-parameter models of a piezo-aeroelastic energy harvester utilizing a dynamic airfoil wing as a base structure for an attached bimorph piezoelectric cantilevered beam. The source of ambient vibration is a wind induced dynamic flutter which was found to initiate at a low airflow speed of 20 m/s and was considered suitable for deployment in both low and high wind speed environment. In adequately assessing the composite piezoelectric beam, the mode shape equation was solved as a damped and forced bimorph cantilevered beam to obtain a more structurally stable system. The dynamic airfoil base and the bimorph piezoelectric cantilever beam were aero-structurally and electromechanically coupled under three different models for electricity generation.

In the analytical model, it was established from the results that the highest voltage, current and power generation occurs at ta load resistance of $R_l = 33\,T\Omega$, $R_l = 0.3\,T\Omega$ and $R_l = 3\,T\Omega$. The maximum generation was obtained at a load resistance of $33\,T\Omega$ when system was excited at short-circuit and open-circuit resonance frequency of 76.5 Hz (mode 1) and 676.5 Hz (mode 3). The system generated a voltage output of $3212\,mV$, a current of $9.39\,mA$, and $0.35\,mW$ for model one (mode 1), model two generated a voltage output of $19210\,mV$, current output of $53.74\,mA$, and power output $32.71\,mW$ (mode 2), and model three produced voltage output of $12400\,mV$, current of $136.10\,mA$, and power output of $12900\,mW$ (mode 3). Hence, piezo-aeroelastic energy harvester in model three gave a substantial improvement in power generation at low wind speed capable of supporting many wireless sensor applications without need for incorporating energy storing device within the system.

REFERENCE

Adhikari, S., Friswell, M. I. and Inman, D. J. (2009). Piezoelectric energy harvesting from broadband random vibrations, *Smart Materials and Structure*, 18(11): 115 - 134.

Alighanbari, H. (1995). *Flutter Analysis and Chaotic Response of an Airfoil Accounting for Structural Nonlinearities*.PhD Thesis, McGill University, Canada.

Alper, E. (2009). *Electromechanical Modelling of Piezoelectric Energy Harvesters* Ph.D. Thesis, Virginia Polytechnic Institute and State University. United States of America (U.S.A.),1-160.

Briscoe, J. and Dunn, S. (2014). *Nanostructured Piezoelectric Energy Harvesters*. McGraw-Hill, New York, 5p.

Erturk, A. and Innam, D. J. (2011). *Piezoelectric Energy Harvesting*.John Wiley &Sons, Delhi, 67-71.

Harne, R. L. and Wang, K. W. (2016). A review of the recent research on vibration energy harvesting via bi-stable systems.*Smart Materials and Structures*, 22(2): 2301.

Hu, Z., Qiu, J., Wang, X., Gao, Y., Liu, X., Chang, Q., Long, Y., and He, X. (2018). An integrated multi-source energy harvester based on vibration and magnetic field energy.*AIP Advances*, 8: 1-9

Jeffrey, A. (1990). *Flutter Evaluation and Control of an Airfoil Solved in the Laplace Domain.*MSc Thesis, McGill University, Canada, 150-151.

Kiran, B., Aleena, P. K., Anumol, C. V., Josnie, A. T. and Nimisha, K. K. (2014). Footstep power generation using piezo electric transducer. *International Journal of Engineering and Innovative Technology (IJEIT)*, 3(10): 264-267.

Ono, S., Miwa, K., Iori, J., Mitsuya, H., Ishibashi, K., Sano, C., Toshiyoshi, H. and Fujita, H. (2016). A novel vibrational energy harvester with electric double layer electrets. *Journal of Physics: Conference Series*. 7(4): 1-4.

Podder, P., Constantinou, P., Amann, A. and Roy, S, (2016). Frequency adjustable MEMS vibration energy harvester. *Journal Physics: Conference Series.* (757): 1-6.

Rizman, Z. I., Yassin I.M., Zaman, F. K., Hashim, F. R., and Yeap, K. H. (2018). Smart multi-application energy harvesting using arduino.*Journal of Fundamental and Applied Science*, (10): 689-704.

Sarker, M., Mohamed, A. and Mohamed, R. (2016). A New Method for a Piezoelectric Energy Harvesting System Using a Backtracking Search Algorithm-based PV Voltage Controller. *Micromachines*, 7(171): 1-16

Zeng, Z., Ren, B., Gai, L., Zhao, X., Luo, H. and Wang, D. (2016). Shear-mode-based cantilever driving low-frequency piezoelectric energy harvester using $0.67Pb(Mg_{1/3}Nb2/3)$ O_3-$0.33PbTiO_3$. *IEEE Transactions on Ultrasonics, Ferroelectrics, and Frequency Control*, 63(8): 1192-1197.

Yuan, M., Cao, Z. and Luo, J. (2018). Characterization, the Influences of Diodes to Piezoelectric Energy Harvester. *International Journal of Smart and Nano Material* (2): 1-16.